Manuscript Number:

Title: Anatomical regurgitant orifice detection and quantification from 3D echocardiographic images

Article Type: Original Contribution

Keywords: Three-dimensional echocardiography; mitral regurgitation; anatomical regurgitant orifice; region competition; max-flow; min-cut.

Corresponding Author: Dr. Miguel Sotaquira, PhD

Corresponding Author's Institution: Universidad de San Buenaventura Bogotá

First Author: Miguel Sotaquira, PhD

Order of Authors: Miguel Sotaquira, PhD; Mauro Pepi; Gloria Tamborini; Enrico Caiani

Abstract: The vena contracta (VC) and the effective regurgitant orifice area (EROA) are currently used for the clinical assessment of mitral regurgitation (MR) from 2D color Doppler imaging. However, these measures are highly user-dependent and with low repeatability and don't represent accurately the anatomic regurgitant orifice (ARO), that is a 3D structure, thus affecting the adequate assessment of MR patients.

We proposed a novel processing method for quantitative assessment of the 3D ARO shape from 3D transesophageal echocardiographic (3D-TEE) datasets, and tested it on a set of 25 patients with MR, compared to ARO manual planimetry. Results show robustness against the user' settings and a high level of agreement compared to manual tracings, thus evidencing the ARO 3D morphology. This highlights the limitations of current clinical approaches, and underlines the importance of ARO shape accurate assessment for diagnosis and treatment of MR patients.

Suggested Reviewers: Oscar Acosta
oscar.acosta@univ-rennes1.fr
Biomedical image processing expertise

Nico Bruining
n.bruining@erasmusmc.nl
Biomedical image processing expertise

Opposed Reviewers:

May 11th, 2016

Prof. Christy K. Holland
Editor-in-Chief
Ultrasound in Medicine and Biology Journal

Dear Prof. Holland,

Here enclosed you can find the manuscript entitled "**Anatomical regurgitant orifice detection and quantification from 3D echocardiographic images**", which we would like to submit for publication in the Ultrasound in Medicine and Biology Journal.

The undersigned corresponding author would like to state that the manuscript has not been submitted elsewhere for publication, that there is no conflict of interest in connection with this manuscript, and that the Institutional Review Board committee of the Centro Cardiologico Monzino in Milan approved the study.

Moreover, each author contributed to this research in its conception and design, data acquisition, analysis and interpretation of data, preparation of the article draft, and final approval of the version we are submitting.

Sincerely,

Miguel Sotaquirá, PhD
Assistant Professor
Faculty of Engineering
Universidad de San Buenaventura
Bogotá (Colombia)

Anatomical regurgitant orifice detection and quantification from 3D echocardiographic images

Miguel Sotaquirá[a,b], Mauro Pepi[c], Gloria Tamborini[c], Enrico G Caiani[b]

[a] Universidad de San Buenaventura Bogotá, Faculty of Engineering

[b] Dipartimento di Elettronica, Informazione e Bioingegneria, Politecnico di Milano, Milan, Italy

[c] Centro Cardiologico Monzino IRCCS, Milan, Italy

Corresponding author:

Miguel Sotaquirá

Universidad de San Buenaventura Bogotá

Cra. 8 H # 172-20

Bogotá, Colombia

Email: msotaquira@usbbog.edu.co, msotaquira@gmail.com

Phone: +573115782114

Abstract

The vena contracta (VC) and the effective regurgitant orifice area (EROA) are currently used for the clinical assessment of mitral regurgitation (MR) from 2D color Doppler imaging. However, these measures are highly user-dependent and with low repeatability and don't represent accurately the anatomic regurgitant orifice (ARO), that is a 3D structure, thus affecting the adequate assessment of MR patients.

We proposed a novel processing method for quantitative assessment of the 3D ARO shape from 3D transesophageal echocardiographic (3D-TEE) datasets, and tested it on a set of 25 patients with MR, compared to ARO manual planimetry. Results show robustness against the user' settings and a high level of agreement compared to manual tracings, thus evidencing the ARO 3D morphology. This highlights the limitations of current clinical approaches, and underlines the importance of ARO shape accurate assessment for diagnosis and treatment of MR patients.

Keywords

Three-dimensional echocardiography; mitral regurgitation; anatomical regurgitant orifice; region competition; max-flow; min-cut.

INTRODUCTION

Valvular heart disease, the damage or alteration in morphology and function of any of the four heart valves, represents an important public health issue. Epidemiologic studies from United States and Europe (Iung, 2003; Nkomo et al., 2006) showed that more than one in eight patients aged 75 and older have moderate or severe valvular disease, a proportion that tends to increase with the projected shift to an older and larger population. These studies stress the importance of early identification and quantification of severity of the disease. Among valvular pathologies, mitral regurgitation (MR) is one of the most common disorders, being a growing public health problem (Enriquez-Sarano et al., 2009).

Current guidelines for the quantitative assessment of MR recommend the use of two-dimensional (2D) color Doppler flow imaging for the estimation of the vena contracta (VC) and the effective regurgitant orifice area (EROA) (Zoghbi et al., 2003; Lancellotti et al., 2010). The VC is defined as the narrowest portion of the regurgitant jet as seen from a 2D cut-plane perpendicular to the commissural line of the valve, whereas the EROA is an indirect measure of the size of the anatomical regurgitant orifice (ARO), and its quantification relies on the assumption that the regurgitant blood flow converges in a hemispherical shape. In spite of being currently used for the assessment of MR severity, the intrinsic 3D nature and the non-circular and non-planar shape of the ARO (Little et al., 2007; 2008; Enriquez-Sarano et al., 2009; Little, 2012) make the estimation of VC diameter and the EROA a highly unreliable and poorly reproducible procedure (Yosefy et al., 2009; Biner et al., 2010; Shanks et al., 2010; Zeng et al., 2011).

The recent advent of 3D color Doppler allows direct planimetry of the regurgitant orifice but it only allows an approximate estimation of the real orifice size, given its non-planar shape (Chandra et al., 2011; Grayburn, 2011). In addition, the correct visualization of the orifice can be affected by user and machine settings, such as color Doppler gain, long ECG-gated multi-beat acquisitions and volume rate, resulting in a user-dependent imaging technique (Little et al., 2008).

Some computational approaches, aimed at semi-automatically segmenting the ARO and reducing user interaction, have been recently proposed (Chandra et al., 2009; 2011; Grady et al., 2011; Moraldo et al., 2013). In (Chandra et al., 2009; 2011) the ARO area from 3D transesophageal echocardiographic (3D-TEE) datasets was computed; the method requires manual tracing of the leaflets followed by the automatic computation of a minimal spanning surface corresponding to the 3D regurgitant orifice. However, the method is time consuming (on average 6 min per dataset) and exhibits low reproducibility. On the other hand Grady et al. (2011) proposed a method that operates directly on the 3D color Doppler dataset that requires one user-defined point to locate the valve, followed by a color segmentation algorithm which allows the estimation of the EROA. In spite of eliminating assumptions about the shape of the regurgitant orifice, custom-made hardware and fine setting of the acquisition parameters are required to achieve accurate results. In another approach, Moraldo et al. (2013) proposed a method for automatically measuring the rate of flow velocity increase with distance using 2D color image segmentation techniques. To ensure a reliable estimation, a total of 40 2D color Doppler frames per patient must me acquired, thus making the method impractical for clinical diagnosis of MR.

To address limitations of previous approaches, we hypothesized that the information contained in the grayscale 3D-TEE data could be processed to quantify the 3D ARO. Accordingly, our aim was to develop a novel method for the semi-automated segmentation and quantification of the 3D ARO from 3D-TEE images, and validate it compared to manual planimetry.

MATERIALS AND METHODS

In Figure 1, a schematic representation of the approach is represented. It is applied on systolic frames (with the valve closed) and uses 3D image and mesh processing procedures to detect the narrowest passage area of the blood flow (corresponding to the 3D ARO). To do so, first a supervised active contour segmentation is applied to the grayscale dataset in order to obtain a 3D polygonal mesh, containing the orifice and surrounding structures. Then, a completely automated procedure, using 3D shape descriptors and a max-flow/min-cut graph-based approach, is used to delineate the ARO 3D contour. Once segmented, a minimal spanning surface representing the 3D ARO surface is computed and several 2D and 3D morphological parameters are calculated.

A. Supervised segmentation of regions located near the 3D ARO

In patients with MR, the regurgitant jet starts on the left ventricle (LV) and gradually constricts until it reaches the ARO, from which it expands radially into the left atrium (LA). In a 3D-TEE image, this regurgitant orifice can be seen as a continuous channel connecting the LA and LV blood pools (Fig. 2). Accordingly, instead of detecting the tissue (mitral leaflets or annulus) in the image, this step focuses on the segmentation of the void regions near the orifice and corresponding to the lower (almost black) intensity voxels containing the regurgitant flow.

To perform this step, a 3D active contour segmentation algorithm was implemented (Zhu and Yuille, 1996; Yushkevich et al., 2006), in which a 3D closed surface iteratively evolves from a user-defined point located near the orifice, allowing the estimation of the structure of interest. This approach ensures that the orifice will always be included in the final segmentation even when the initial seed contains both the tissue and the void region.

The 3D surface evolution is controlled by the sum of internal and external forces:

$$F = \alpha(P_{obj} - P_{bkg}) + \beta\kappa \qquad (1)$$

The internal force $\beta\kappa$ is proportional to the mean curvature k of the surface, whereas the external force term $\alpha(P_{obj} - P_{bkg})$ describes the *probability map* (Fig. 3) indicating the probability that a voxel belongs to the object of interest or to the background. This *probability map* is the result of a smooth threshold applied to the original 3D-TEE volume and defined as a sigmoid function:

$$I_{out} = 1 - \frac{2}{1 + e^{-\frac{I_{in} - \mu}{\sigma}}} \qquad (2)$$

where I_{in} represents the original grayscale 3D-TEE image, μ defines the intensity around which the transformation is centered, σ is a smoothing parameter defining how steep the sigmoid curve is, and I_{out} represents the desired *probability map* with intensity values ranging from -1 to 1. During validation a set of proper α, β, μ and σ parameters was empirically established so as to ensure correct segmentation results (Table 1, Results, Section A).

Once computed the *probability map*, a 3D surface containing the orifice is obtained. Next, the marching cubes algorithm (Lorensen and Cline, 1987) is used to compute a 3D polygonal mesh representation of the regions near the orifice. This structure is defined as the *partial void* (Fig. 4) which, regardless of the shape of the orifice, can be described as two convex shapes (the *cavities*, corresponding to the partial segmentation of the atrium and the ventricle) connected by a narrower structure (the *channel*, containing the regurgitant orifice). The advantage of using this approach is that the segmented structures exhibit similar characteristics even for patients with different types of MR. This *partial void* satisfies several geometrical priors, as shown in Fig. 4:

(i) The *cavities* are larger than the *channel;*

(ii) The *channel* is located towards the middle section of the *partial void*;

(iii) The *cavities* are convex shapes;

(iv) The *channel* can be narrow (Fig. 4, left) or wide (Fig. 4, right), but in any case it will satisfy the geometrical prior (i).

B. Automatic segmentation of the 3D ARO contour

In this step, the 3D contour of the ARO was automatically segmented from the *partial void* mesh using the the max-flow/min-cut algorithm (Boykov and Kolmogorov, 2004). From graph theory, when the maximum flow between two nodes of a directed graph is obtained, a set of graph edges becomes saturated (i.e., min-cut), and it separates the graph into two disjoint subsets. In the context of this problem, if the *partial void* mesh is represented as a directed graph, and additionally if a pair of *source* and *sink* nodes are added and the edge capacities are properly defined, then it is possible to compute the min-cut that will correspond to the narrowest portion of the *partial void* (i.e. the 3D ARO contour). To successfully obtain this contour, three steps must be performed: computation of edge capacities, computation of *source* and *sink* nodes, and estimation of 3D ARO contour using the max-flow/min-cut algorithm.

Computation of edge capacities. The shape diameter function (SDF) (Shapira et al., 2008) was used to compute edge capacities. The SDF is a scalar function, defined on the mesh surface, which represents the diameter of the object's volume in the neighborhood of each vertex in the mesh. In the context of the *partial void*'s mesh, the SDF is a measure of how broad or narrow is a structure, thus allowing the enhancement of the *channel* that contains the ARO. The algorithm relies on a ray-tracing point-mesh intersection procedure: for each vertex on the surface, a cone centered on its inward unit normal is defined. Then, several rays inside this cone are traced and the intersection of each ray with the mesh is computed. SDF estimation requires the definition of two parameters, the cone angle and the number of rays to be traced, which affect both the accuracy in the estimation of the diameters as well as computation time. In our implementation, a cone angle of 30º and a total of 30 rays were empirically chosen for SDF computation. These settings provided a good enhancement of the *channel* and kept the computation time acceptable (about 15 sec for meshes with 30000 vertices).

Fig. 5 shows an example of SDF computation applied to a *partial void*. As seen from this figure, the SDF provides a detailed enhancement of the *channel* (the dark blue ribbons in Fig. 5), which exhibits lower diameters (lower SDF values) when compared with those of the *cavities* (higher values, in red in Fig. 5).

Computation of source and sink nodes. These nodes correspond to the vertices in the mesh located on the most distal region of each *cavity*, and can be computed using the information provided by the average geodesic distance (AGD) scalar field (Zhang et al., 2005). The AGD is a measure of the degree of separation of each vertex in the mesh, where vertices near the center of the mesh, closer to other vertices, exhibit lower AGD values, whereas vertices away from the mesh's center will have higher values (Fig. 6a).

Once computed the AGD, a set of *feature points* corresponding to the local maxima of the AGD function (red dots in Fig. 6b) is obtained following the procedure described by Katz et al. (Katz et al., 2005). In order to obtain only two points, one for each *cavity* and corresponding to the *source* and *sink* nodes, two additional criteria were introduced:

(1) the *source* vertex will be the *feature point* with the highest AGD value and (2) the *sink* vertex will be the *feature point* located at the maximum Euclidean distance from the *source* vertex. When applied, these criteria allow the correct computation of the *source* and *sink* nodes, as shown in Fig. 6c.

Segmentation of the 3D ARO contour using graph-cuts. A directed graph was first generated from the *partial void* mesh; this graph consists of a set of nodes corresponding to each vertex on the mesh and a set of directed edges going from the *source* to the *sink* vertex. The edge capacities were defined using the SDF scalar field values; to ensure that the min-cut will lie at the ARO location, especially in noisy meshes, the set of SDF scalar values was first transformed using a non-linear function:

$$sdf_T(v_i) = e^{\left[\frac{sdf(v_i)}{sdf_{\min}} - 1\right]} - 1 \qquad (3)$$

where sdf_{min} is the global minimum of the SDF field and $sdf(v_i)$ is the value of the SDF field at vertex v_i. This transformation ensures that values closer to the global minimum (located near the ARO, within the *channel*) will have transformed values closer to zero.

Next, the edge capacities $C_{vi,vj}$ were simply defined as:

$$C_{v_i,v_j} = sdf_T(v_i) + sdf_T(v_j) \qquad (4)$$

Using this formulation, the edge capacities in the *channel* will be characterized by lower values, thus forcing the min-cut to lie on the ARO.

Fig. 7 depicts some examples of the resulting ARO segmented contours on *partial voids* with different geometries. It is worth noting that, in all cases, each contour matches the location of the lower SDF values, which in turn represent the 3D ARO contour.

Given the noise in the mesh, usually a 'jagged' contour is obtained (Fig. 8, left). By applying a cubic-spline interpolation to the points in the initial contour a smooth representation of the 3D ARO boundary is obtained(Fig. 8, right). This smooth contour served as the input for the quantification stage.

C. 2D and 3D morphological quantification of the ARO.

Given the non-planar shape of the computed 3D contour (as seen in Fig. 8), the minimal surface area spanning its boundary was obtained as a representation of the ARO surface. This minimal surface can be computed by using the "stretched membrane" approximation and solving the biharmonic equation (Chandra et al., 2011). The thin-plate splines represent the fundamental solution to this equation (Bookstein, 1989); by applying this interpolation on the sparse set of points defining the 3D contour, the corresponding 3D ARO surface can be obtained. Fig. 9 shows three examples of the computed 3D ARO for three different patients, where it is evident that none of these surfaces is planar nor circular.

From this representation, several morphological parameters were then computed: (1) 3D surface area and its 2D projected area, computed from the triangulation of the 3D ARO minimal surface; (2) planarity index, defined as the ratio between the 2D and the 3D areas (values closer to 1 represent more planar orifices); (3) circularity index, defined as the ratio between the minimum and the maximum axes, obtained by first projecting the 3D ARO onto its best-fit plane and then fitting it to an ellipse (values closer to 1 represent more circular orifices).

RESULTS

The initial segmentation of the *partial void* was performed using ITK-SNAP (Yushkevich et al., 2006), whereas the remaining automatic steps were implemented using the open source programming libraries VTK (Visualization Toolkit) and iGraph. The active contour segmentation required 1 min on average, whereas the automatic computation of the ARO contour and its morphological parameters required on average 50 sec. Thus, the complete segmentation and quantification of the 3D ARO was achieved in roughly 2 min.

A. Sensitivity study

Fig. 10 shows the sensitivity of the results to the different setting of the user-defined parameters. It is possible to observe that, in the range of examined values, the highest CVs are related to the 3D surface area parameter, in the order of 5%. In particular, the location of the initialization point ($\boldsymbol{x}$) represents the main determinant of variation, while the sigmoid smoothness parameter (σ) is the least. From the results of the sensitivity analysis, the values of the active-contour parameters were set as summarized in Table 1, for the subsequent analyses.

B. Reproducibility of manual planimetry.

Table 2 summarizes the reproducibility of ARO parameters, expressed as intra-observer variability resulting from two blinded manual tracings of the 25 patients included in the analysis. The CV was below the 12% limit in most cases (19 out of 25) for the ARO 2D area, whereas for the ARO circularity index the CVs were below 11.1% in all cases.

Fig. 11 is an example of visual comparison between different orifices manually traced by the expert and the corresponding 2D view of the same orifice resulting from the segmentation, where it is possible to appreciate a good morphological correspondence.

Figures 12 and 13 show the results of the linear regression and Bland-Altman analyses. The ARO 2D areas (Fig. 12) exhibited good correlations and small biases ($p<0.05$, paired t-test with zero values) and narrow CI with the reference measurements, both for the combined groups and for FMR and MVP separately, with no statistically significant differences. For the ARO circularity index (Fig. 13), the comparison resulted in high correlation, small biases and narrow limits of agreement, and no significant differences were found when comparing both measures.

C. Morphological characterization of the 3D ARO.

Table 3 shows the median, 25% and 75% percentiles of the 3D and 2D ARO areas, planarity and circularity indices for all patients and for each group. In the combined group, the ARO 3D surface area varied between 0.01 cm^2 and 0.71 cm^2, while the range for the 2D projected area was between 0.01 cm^2 and 0.62 cm^2; significant differences were found when comparing 3D and 2D areas in all cases.

Regarding the circularity index, only one patient presented an almost rounded ARO (0.92), whereas the remaining patients had indices below 0.82; the resulting median values of 0.62 and 0.56 for the FMR and MVP groups respectively imply in both cases highly elongated AROs. The non-planarity of ARO was confirmed by the computed planarity index: only 6/25 patients had an index above 0.9 with values ranging from 0.49 to 0.94, whereas significant differences were found between the pathologic groups, with the *MVP* exhibiting more non-planar ARO than *FMR* (median values of 0.77 vs 0.90).

DISCUSSION

We presented a novel algorithm, with minimal user interaction, that allows the quantification of the 3D ARO from 3D-TEE datasets based on segmentation of the void regions containing the regurgitant flow.

A. Validation

The sensitivity study suggests that the method is robust to variation in the setting of the parameters for the segmentation using region competition. The results shown in Section 3.A evidence that the location of the user-specified point is the parameter that most significantly affects the repeatability of the algorithm, but the variability observed in this case is of only 5%. The remaining parameters (threshold, smoothness, curvature and balloon force) have a less significant impact on the variability of computed morphological parameters, with CVs of around 3% or less.

The manual planimetry performed by the expert revealed a low reproducibility, with CVs in the range [3.2-21.3]% (Table 2), much higher than the highest variability obtained with the proposed method (close to 5% and owed to the location of the user-specified point as shown in Fig. 10). A high level of agreement between the computed ARO 2D area and the reference values obtained using manual planimetry of the orifice was also observed, thus confirming the reliability of the proposed approach as a tool for the ARO shape estimation. The level of agreement was even higher when the circularity index was considered, which can be explained by the fact that this index represents the ratio between the minor and major axes of the 2D ARO. An overestimation of the ARO 2D area resulting from an increased length in both axes is masked once the ratio is computed, thus explaining the obtained zero biases, and the narrow limits of agreement.

Based on the fact that the 2D parameters computed from the 3D ARO are in agreement with the manual reference, we hypothesize that also the 3D parameters are accurate in representing the 3D ARO morphology. Comparison of computed 3D versus 2D area in the two groups of patients showed a significant underestimation of the latter, in particular in MVP patients characterized by a larger and more non-planar orifice, not quantifiable with conventional 2D planimetry. This can be explained by the complex morphology of the channel in the prolapsed valves, where instead of "non-touching" leaflets (as in functional MR), their overlapping is present. This finding confirms previous observations (Grayburn, 2011) and poses a question on potential inaccuracy in the current approaches for the ARO assessment using planimetry in 3D-TEE and cardiac magnetic resonance (Buchner et al., 2008; Yosefy et al., 2009; Shanks et al., 2010).

B. Strengths of the algorithm and comparison with other approaches.

The successful segmentation of the ARO lies in the max-flow/min-cut algorithm, which allows the computation of a closed connected contour representing its boundary. As discussed in Section 2, the SDF (Shapira et al., 2008) is a robust mesh feature that, when computed on the partial void mesh, allows the enhancement of the *channel* that contains the ARO. By representing the 3D triangular mesh as a graph and properly defining a pair of *source* and *sink* nodes as well as its edge capacities, the max-flow/min-cut algorithm can be applied. Since the edges near the ARO have low capacities (given their dependence on the SDF values), once reached the maximum flow those edges will easily be saturated, which corresponds by definition (Boykov and Kolmogorov, 2001) to the minimum cut.

When compared with other approaches, the proposed methodology overcomes many of the previous limitations. In contrast to the works of Chandra et al (Chandra et al., 2011) our method relies on minimal user intervention (during the active contour segmentation of the *partial void*), together with reduced computation time, allowing the quantification of the 3D ARO in about 2 min, with the capability of segmenting orifices both in MV with functional MR or prolapse. Moreover, differently from Moraldo et al. (2013), only one 3D-TEE systolic frame is required to compute the 3D ARO, without making any assumptions about the orifice shape. In addition, our algorithm makes use of existent technologies for the acquisition of 3D-TEE datasets, and the segmentation is directly applied on the voids in the images representing the underlying anatomical structures containing the regurgitant orifice, with no need to acquire color-Doppler 3D images as proposed by Grady et al. (2011).

Although not tested in the studied population, our algorithm could also potentially capable of quantifying the total regurgitant area in MV with multiple regurgitant jets. In such configurations, each ARO can be separately segmented using the proposed approach and then the individual contributions can be summed up. Such computation is not possible using the standard EROA approach, since the superposition of regurgitant jets makes difficult the visualization of individual regurgitant jets in the color Doppler image.

C. Clinical implications

Underestimation of ARO area could have profound implications in the diagnosis of patients with MR. Current guidelines (Zoghbi et al., 2003; Lancellotti et al., 2010) for the assessment of MR severity relies on the quantification of both VC and EROA using 2D color Doppler imaging. As EROA assumes a planar and circular orifice in its computation, this could lead to misclassification of MR severity with potential effects in patient treatment. For example, if a planarity index of 0.5 (the lowest value found in the studied population) is assumed, this implies that the real size of the regurgitant orifice would be in fact twice that of the EROA if measured using the flow convergence method.

Another important observation is that, regardless of the MR etiology, whether it is functional or organic (as in MVP patients), almost all orifices (24 out of 25) in the studied population had a non-circular shape (Table 3). This is in agreement with previous studies that used planimetry to evaluate the regurgitant orifice (Little et al., 2008; Enriquez-Sarano et al., 2009; Little, 2012), and again challenges the current standard clinical approaches that rely on the assessment of both the VC width and the effective regurgitant orifice area via 2D color Doppler imaging and the flow convergence method, that rely on the assumption of a circularly symmetric and planar regurgitant orifice.

D. Limitations.

The main limitation of the proposed approach is the absence of a proper gold standard for the comparison of the results on the ARO 3D morphology. For this reason, we used clinically accepted ARO 2D planimetry as reference values for comparison. Despite the resulting high correlation in 2D, we cannot ensure that the computed 3D contour and the derived parameters completely correspond to the true regurgitant orifice. However, our findings in two groups of patients with different etiology, including non-circularity and non-planarity ARO indices, further stressed limitations in current clinical guidelines, suggesting that the proposed approach could be a more reliable tool in the assessment of MR severity, given the additional third dimension in the computed parameters.

CONCLUSIONS

A new method for the semi-automatic quantification of the 3D ARO was presented and preliminary validated. In this approach, the user only had to select an initial threshold and one point near the regurgitant orifice. From this initialization, a 3D mesh containing the regurgitant orifice was obtained, and a max-flow/min-cut graph segmentation algorithm allowed the automatic detection of the 3D ARO contour an its morphological characterization, including the computation of the 3D surface area, its circularity and planarity indices. The proposed algorithm is capable of delineating the 3D ARO both in valves with functional mitral regurgitation or with degenerative MV disease. For these reasons, it could provide a more reliable assessment of the severity of mitral regurgitation when compared with current approaches, such as 2D planimetry or the quantification of the VC or the EROA using conventional 2D color Doppler imaging.

REFERENCES

Biner, S., Rafique, A., Rafii, F., Tolstrup, K., Noorani, O., Shiota, T., Gurudevan, S., Siegel, R.J. Reproducibility of Proximal Isovelocity Surface Area, Vena Contracta, and Regurgitant Jet Area for Assessment of Mitral Regurgitation Severity. J Am Coll Cardiol Cardiovasc Imaging 2010; 3:235–43.

Bookstein, F.L. Principal Warps: Thin-Plate Splines and the Decomposition of Deformations. IEEE Trans Patt An Mach Intell 1979; 11:567–85.

Boykov, Y., Kolmogorov, V. An experimental comparison of min-cut/max-flow algorithms for energy minimization in vision. IEEE Trans Patt An Mach Intell 2004; 26(9):1124-37.

Buchner, S., Debl, K., Poschenrieder, F., Feuerbach, S., Riegger, G.A.J., Luchner, A., Djavidani, B. Cardiovascular Magnetic Resonance for Direct Assessment of Anatomic Regurgitant Orifice in Mitral Regurgitation. Circulation Cardiovasc Imaging 2001; 1:148–55.

Chandra, S., Salgo, I.S., Sugeng, L., Weinert, L., Settlemier, S.H., Mor-Avi, V., Lang, R.M. A three-dimensional insight into the complexity of flow convergence in mitral regurgitation: adjunctive benefit of anatomic regurgitant orifice area. Am J Physiol 2011; 301:H1015–24.

Chandra, S., Weinert, L., Sugeng, L., Salgo, I.S., Settlemier, S., Shen, J.X., Mor-Avi, V., Lang, R. Volumetric Measurement of the Anatomic Regurgitant Orifice Area in Mitral Regurgitation: Comparison with Two-Dimensional Flow Convergence Analysis. Comput in Cardiol 2009; 36:769–72.

Enriquez-Sarano, M., Akins, C.W., Vahanian, A. Mitral regurgitation. Lancet 2009 373:1382–94.

Grady, L., Datta, S., Kutter, O., Duong, C. Regurgitation quantification using 3D PISA in volume echocardiography. MICCAI Proceedings 2011; 512–19.

Grayburn, P.A. The Importance of Regurgitant Orifice Shape in Mitral Regurgitation. J Am Coll Cardiol Cardiovasc Imaging 2011; 4: 1097–99.

Iung, B. A prospective survey of patients with valvular heart disease in Europe: The Euro Heart Survey on Valvular Heart Disease. Eur Heart J Cardiovasc Imaging 2003; 24:1231–43.

Katz, S., Leifman, G., Tal, A. Mesh segmentation using feature point and core extraction. Vis Comput 2005; 21:649–58.

Lancellotti, P., Moura, L., Pierard, L.A., Agricola, E., Popescu, B.A., Tribouilloy, C., Hagendorff, A., Monin, J.L., Badano, L., Zamorano, J.L. European Association of Echocardiography recommendations for the assessment of valvular regurgitation. Part 2: mitral and tricuspid regurgitation (native valve disease). Eur J Echocardiography 2010; 11:307–32.

Little, S.H., The Vena Contracta Area. J Am Coll Cardiol Cardiovasc Imaging 2012; 5:677–80.

Little, S.H., Igo, S.R., Pirat, B., McCulloch, M., Hartley, C.J., Nosé, Y., Zoghbi, W.A. In Vitro Validation of Real-Time Three-Dimensional Color Doppler Echocardiography for Direct Measurement of Proximal Isovelocity Surface Area in Mitral Regurgitation. Am J Cardiol 2007; 99:1440–47.

Little, S.H., Pirat, B., Kumar, R., Igo, S.R., McCulloch, M., Hartley, C.J., Xu, J., Zoghbi, W.A. Three-dimensional color Doppler echocardiography for direct measurement of vena contracta area in mitral regurgitation: in vitro validation and clinical experience. J Am Coll Cardiol Cardiovasc Imaging 2008; 1:695–704.

Lorensen, W., Cline, H. Marching cubes: a high resolution 3D surface construction algorithm. ACM siggraph comput graphics 1987; 21:163–69.

Moraldo, M., Bergamini, C., Malaweera, A.S.N., Dhutia, N.M., Pabari, P.A., Willson, K., Baruah, R., Manisty, C., Davies, J.E., Xu, X.Y., Hughes, A.D., Francis, D.P. A novel fully automated method for mitral regurgitant orifice area quantification. Int J Cardiol 2013; 166:688–95.

Nkomo, V.T., Gardin, J.M., Skelton, T.N., Gottdiener, J.S., Scott, C.G., Enriquez-Sarano, M. Burden of valvular heart diseases: a population-based study. Lancet 2006; 368: 1005–1011.

Shanks, M., Siebelink, H.M.J., Delgado, V., van de Veire, N.R.L., Ng, A.C.T., Sieders, A., Schuijf, J.D., Lamb, H.J., Ajmone Marsan, N., Westenberg, J.J.M., Kroft, L.J., de Roos, A., Bax, J.J. Quantitative Assessment of Mitral Regurgitation: Comparison Between Three-Dimensional Transesophageal Echocardiography and Magnetic Resonance Imaging. Circulation Cardiovasc Imaging 2010; 3:694–700.

Shapira, L., Shamir, A., Cohen-Or, D. Consistent mesh partitioning and skeletonisation using the shape diameter function. Visual Comput 2008; 24:249–59.

Yosefy, C., Hung, J., Chua, S., Vaturi, M., Ton-Nu, T.-T., Handschumacher, M.D., Levine, R.A. Direct Measurement of Vena Contracta Area by Real-Time 3-Dimensional Echocardiography for Assessing Severity of Mitral Regurgitation. Am J Cardiol 2009; 104:978–983.

Yushkevich, P.A., Piven, J., Hazlett, H.C., Smith, R.G., Ho, S., Gee, J.C., Gerig, G. User-guided 3D active contour segmentation of anatomical structures: significantly improved efficiency and reliability. NeuroImage 2006; 31:1116–28.

Zeng, X., Levine, R.A., Hua, L., Morris, E.L., Kang, Y., Flaherty, M., Morgan, N.V., Hung, J. Diagnostic Value of Vena Contracta Area in the Quantification of Mitral Regurgitation Severity by Color Doppler 3D Echocardiography. Circulation Cardiovasc Imaging 2011; 4:506–513.

Zhang, E., Mischaikow, K., Turk, G. Feature-Based Surface Parameterization and Texture Mapping. ACM Trans Graphics 2005; 24:1–27.

Zhu, S.C., Yuille, A. Region Competition: Unifying Snakes, Region Growing and Bayes/MDL for Multiband Image Segmentation. IEEE Trans Patt An Mach Intell 1996; 18:884–900.

Zoghbi, W.A., Enriquez-Sarano, M., Foster, E., Grayburn, P.A., Kraft, C., Levine, R.A., Nihoyannopoulos, P., Otto, C.M., Quinones, M.A., Rakowski, H., Stewart, W.J., Waggoner, A., Weissman, N.J. Recommendations for evaluation of the severity of native valvular regurgitation with two-dimensional and doppler echocardiography. J Am Soc Echocardiogr 2003; 16:777–802.

FIGURES CAPTION LIST

Fig. 1. Flow chart of the proposed algorithm for 3D ARO segmentation and quantification

Fig. 2. A 2D cut-plane, taken from a systolic frame in the 3D-TEE image, depicting the location of the left atrium (LA) and ventricle (LV) as well as the presence of the regurgitant orifice (in red). Notice that the blood pool in the image corresponds to the darkest regions in the image

Fig. 3 . 2D cut-plane corresponding to the computed probability map probability. In this map the void regions exhibit values close to 1 (in white). LA: left atrium, LV: left ventricle

Fig. 4. Schematic definition of the channel, cavities and partial void in two cases with different morphology

Fig. 5. An example of a computed SDF scalar field, with the *channel* exhibiting lower SDF values (closer to 2.0 mm) when compared to those of the *cavities* (closer to 30.0 mm)

Fig. 6. Steps involved in the computation of *source* and *sink* nodes. (a) AGD scalar field; (b) Computed *feature points*; (c) Computed *source* and *sink* nodes

Fig. 7. Examples of the automatically computed 3D ARO contours (in red) using the max-flow/min-cut algorithm in four different valves. The color map on each mesh represents the computed SDF scalar field (with blue regions corresponding to the lower values),

whereas the red contours represent the computed min-cut. Notice the direct correspondence between each contour and the local minima in the SDF field

Fig. 8. Left: an initial ‘jagged’ contour is obtained from the min-cut segmentation. Right: the smooth ARO contour after cubic-spline interpolation

Fig. 9. Lateral (first row) and top (second row) views of three computed 3D ARO surfaces

Fig. 10. Dependency of the CV on the setting of the active contour parameters $(\mu, \sigma, \alpha, \beta, \boldsymbol{x})$ for 3D surface area, circularity and planarity indices computation

Fig. 11. Three examples of comparing the 2D contour obtained from planimetry (in yellow) with a 2D atrial view of the automatically computed 3D ARO (gray shape on the right of each panel)

Fig. 12. Comparison between the computed ARO 2D areas and the reference measurements, performed in all patients and on each group separately. Left column: linear regression; right column: Bland-Altman analysis

Fig. 13. Comparison between the computed ARO 2D circularity index and the reference measurements, performed in all patients and on each group separately. Left column: linear regression; right column: Bland-Altman analysis. a.u.: adimensional units

TABLES

Parameter	*Range/value*
μ: Threshold (expressed as a percentage of the maximum grayscale value in the 3D-TEE image)	[10%-40%]
σ: Smooth of the sigmoid	3.0
α: Balloon force coefficient	1.0
β: Curvature force coefficient	0.4

Table 1. Setting of the active contour segmentation parameters used for computing the *partial void*

	Valve	**ARO 2D area**		**ARO circularity index**	
		Mean (cm^2)	**CV (%)**	**Mean (a.u.)**	**CV (%)**
FMR group	1	0.48	11.0	0.12	4.4
	2	0.28	6.4	0.32	6.9
	3	0.03	18.6	0.68	8.5
	4	0.02	21.3	0.70	8.2
	5	0.18	7.4	0.60	6.7
	6	0.19	9.2	0.45	3.2
	7	0.25	8.3	0.58	9.5
	8	0.06	20.1	0.72	8.4
	9	0.01	16.0	0.86	8.9
	10	0.26	10.2	0.98	9.7
	11	0.10	13.3	0.26	6.2
	12	0.22	9.2	0.25	5.3

MVP group	13	0.28	5.0	0.60	3.8
	14	0.16	8.7	0.90	6.3
	15	0.41	10.3	0.30	9.2
	16	0.13	11.1	0.78	8.5
	17	0.14	8.3	0.58	5.2
	18	0.17	9.5	0.50	5.5
	19	0.23	11.8	0.63	6.1
	20	0.15	6.7	0.61	9.1
	21	0.16	4.7	0.38	3.9
	22	0.01	19.0	0.99	8.3
	23	0.21	10.1	0.43	11.1
	24	0.32	9.5	0.49	8.0
	25	0.21	9.7	0.49	8.4

Table 2. Reproducibility results for the manual planimetry

Group **Parameter**	**All patients**	**FMR**	**MVP**
3D ARO surface area (cm^2)	0.21 (0.13; 0.38)	0.13 (0.09; 0.42)	0.30 (0.17; 0.33)
2D ARO projected area (cm^2)	0.16 (0.11; 0.28)*	0.12 (0.08; 0.38)*	0.17 (0.13; 0.27)*
Planarity index (a.u.)	0.80 (0.77; 0.90)	0.90 (0.84; 0.92)	0.77 (0.66; 0.78) **
Circularity (a.u.)	0.57 (0.38; 0.66)	0.62 (0.36; 0.68)	0.56 (0.50; 0.60)

* $p<0.01$ 2D vs. 3D ARO surface area, Student's paired t-test

** $p<0.01$ vs. FMR, Mann-Whitney U test

Table 3. Comparison of computed 3D and 2D parameters from the 3D ARO, in all patients and in FMR and MVP groups.

Figure 1

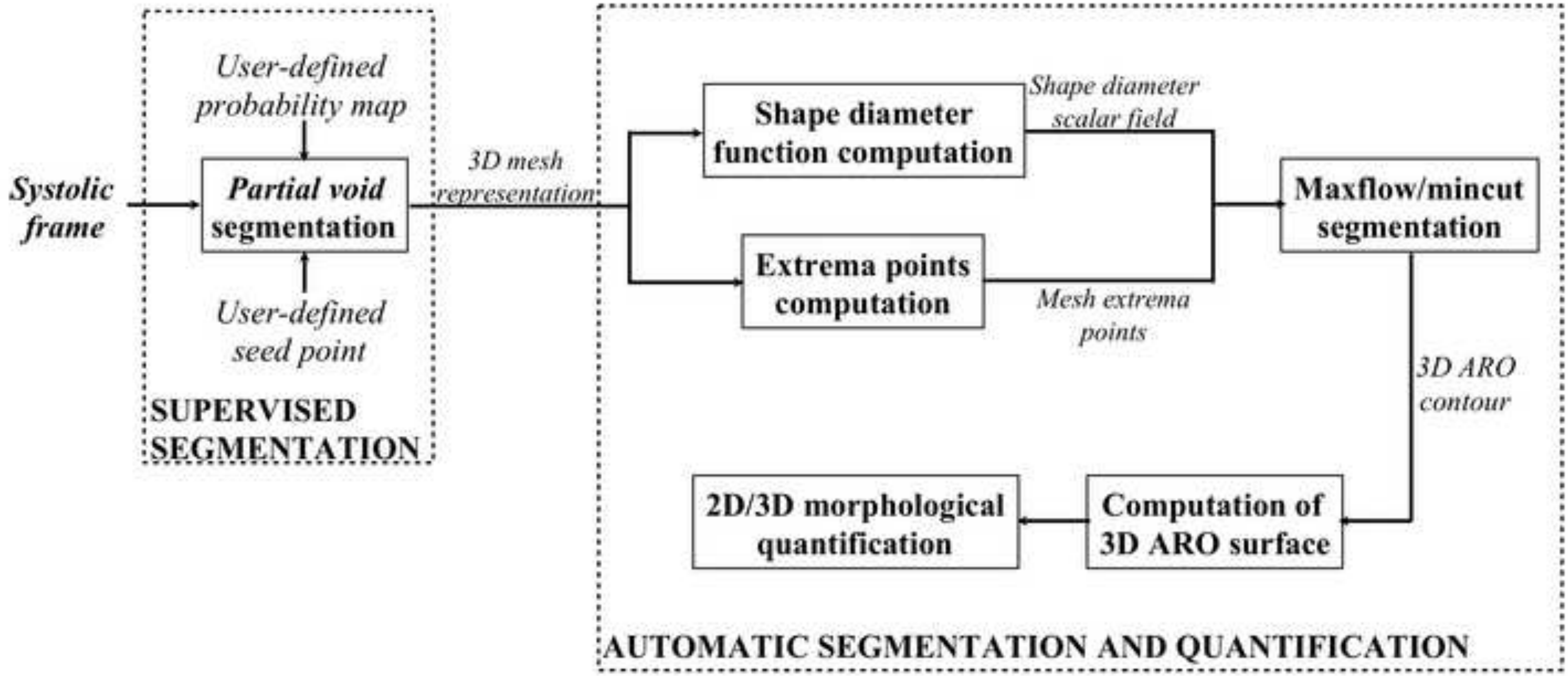
Systolic frame
User-defined probability map
Partial void segmentation
User-defined seed point
SUPERVISED SEGMENTATION
3D mesh representation
Shape diameter function computation
Shape diameter scalar field
Extrema points computation
Mesh extrema points
Maxflow/mincut segmentation
3D ARO contour
Computation of 3D ARO surface
2D/3D morphological quantification
AUTOMATIC SEGMENTATION AND QUANTIFICATION

Figure 2

Click here to download high resolution image

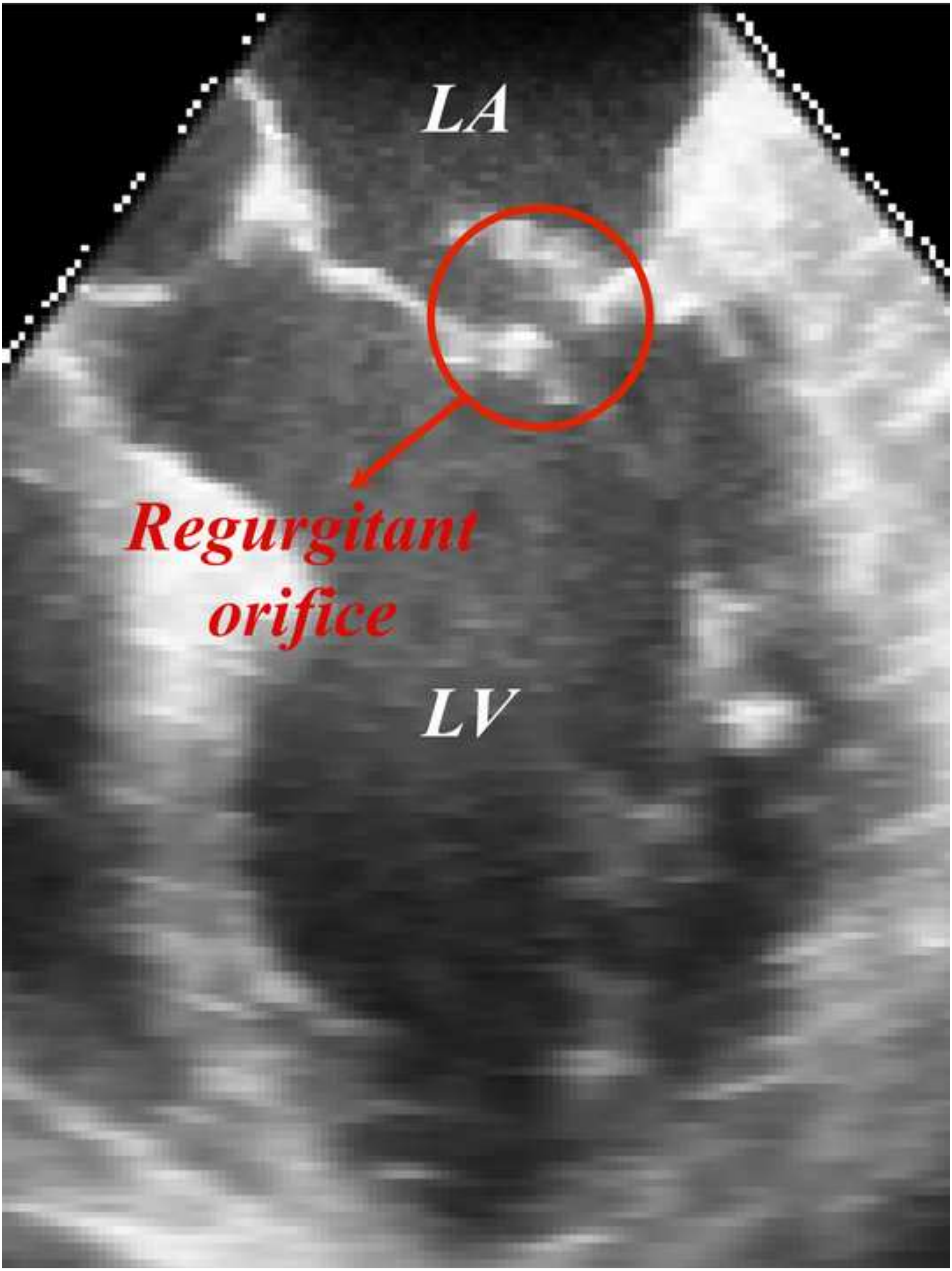

Figure 3

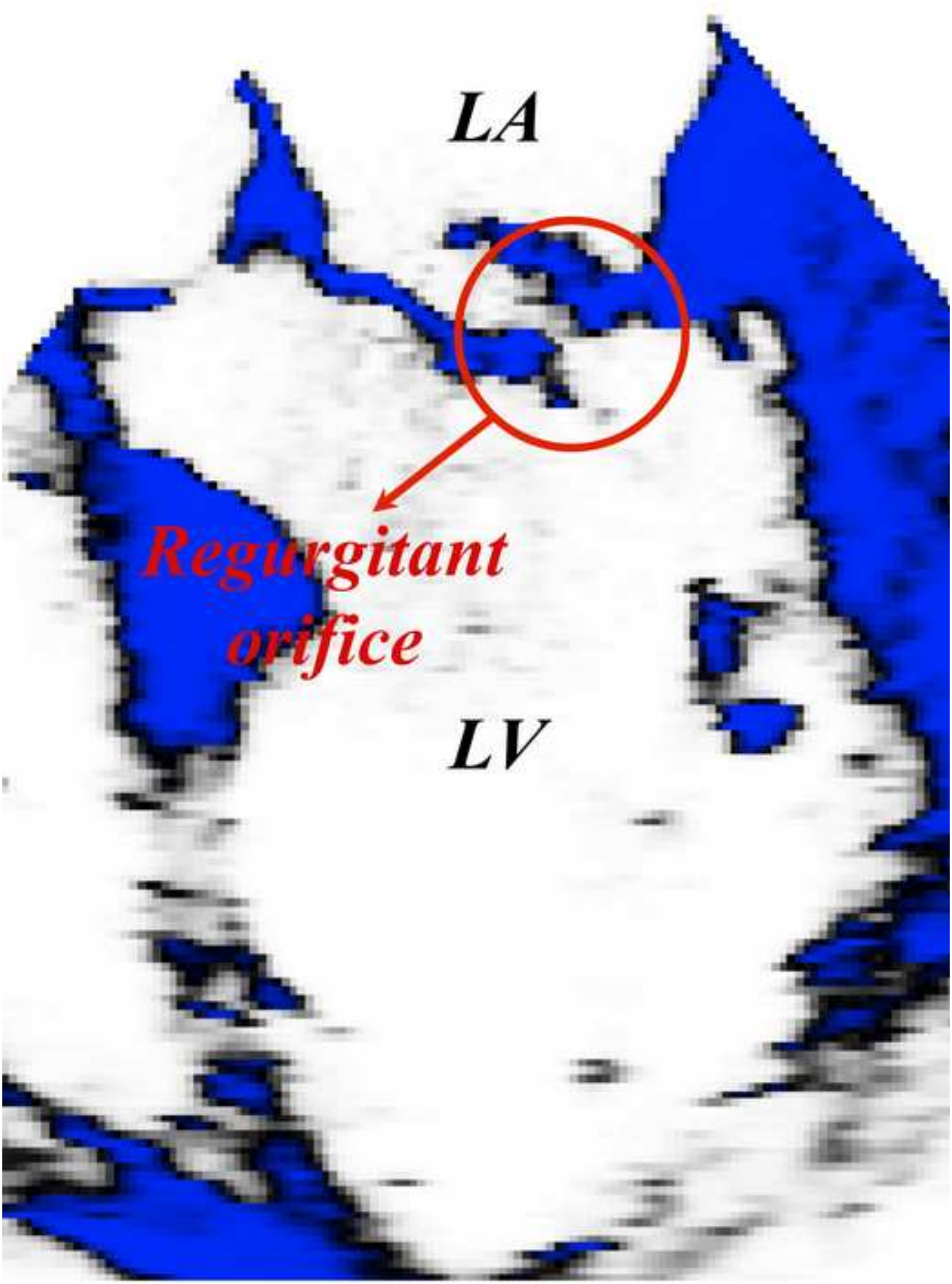

Figure 4

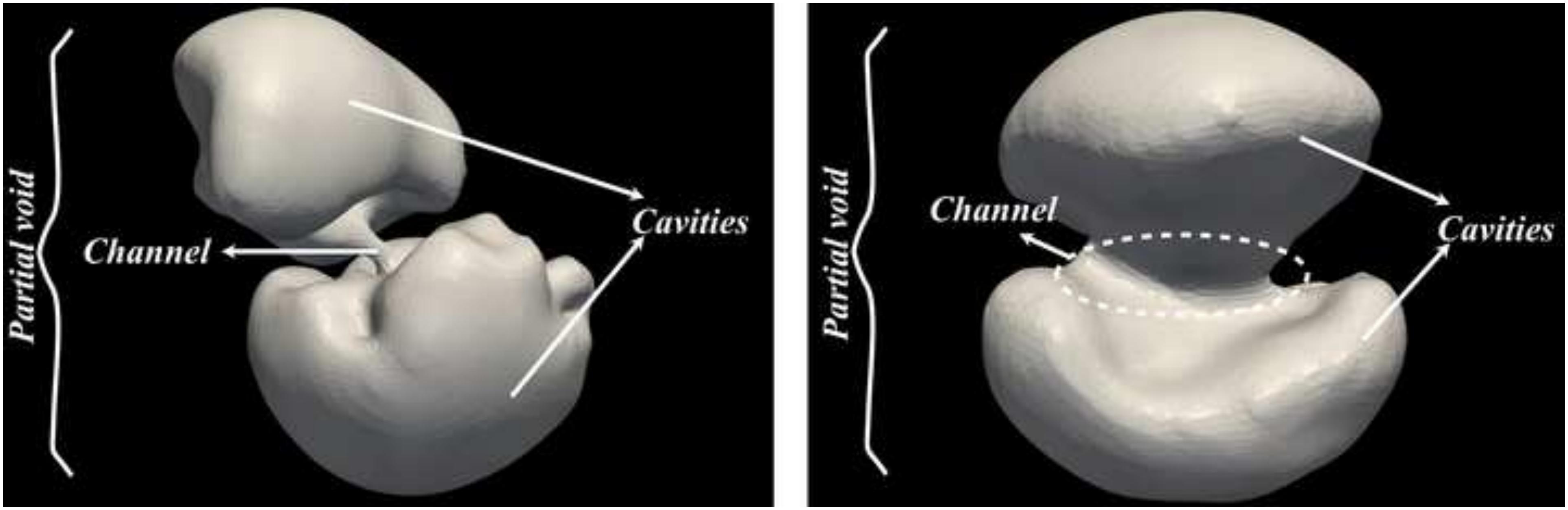
Partial void
Channel
Cavities
Partial void
Channel
Cavities

Figure 5

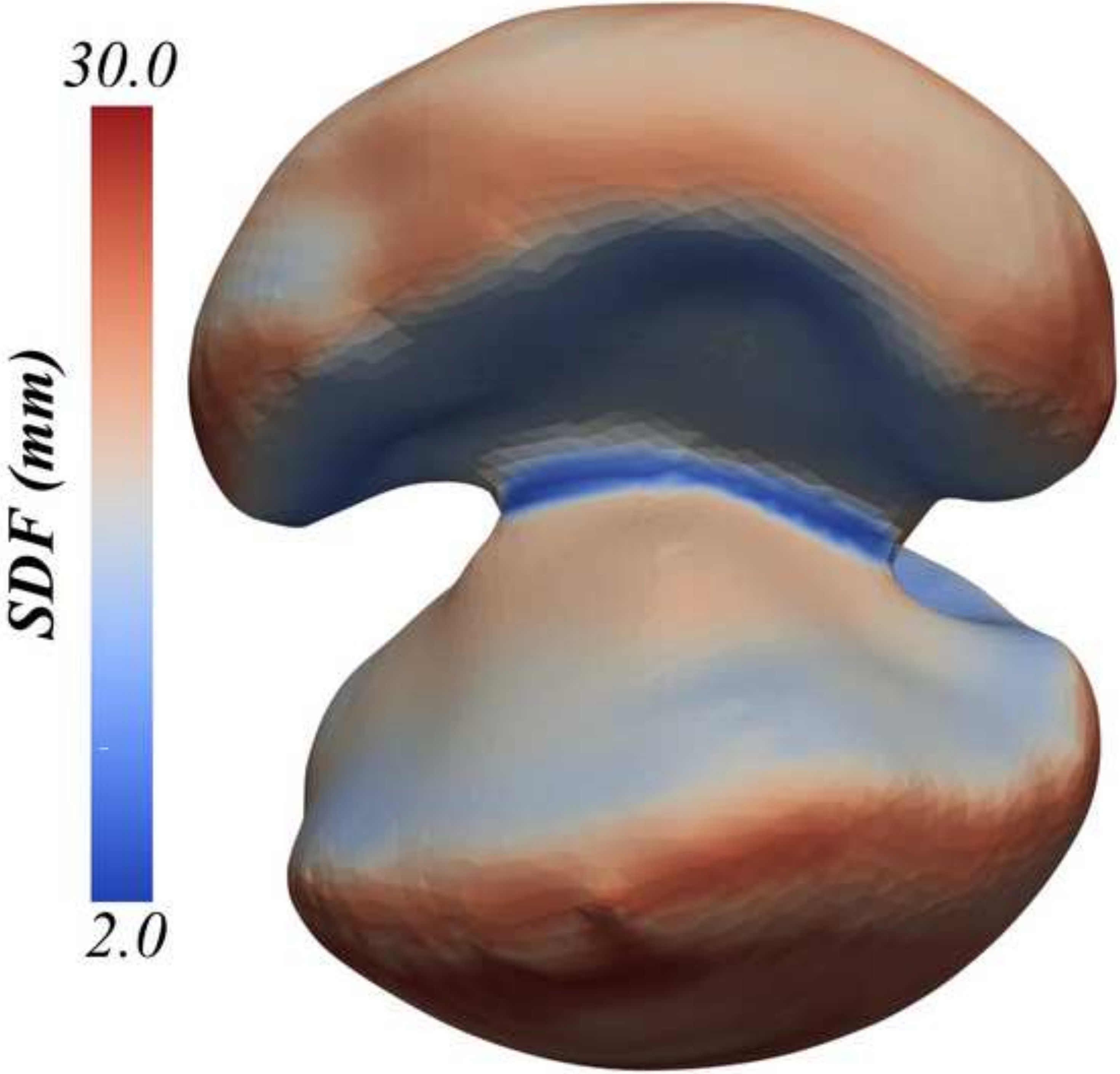

Figure 6

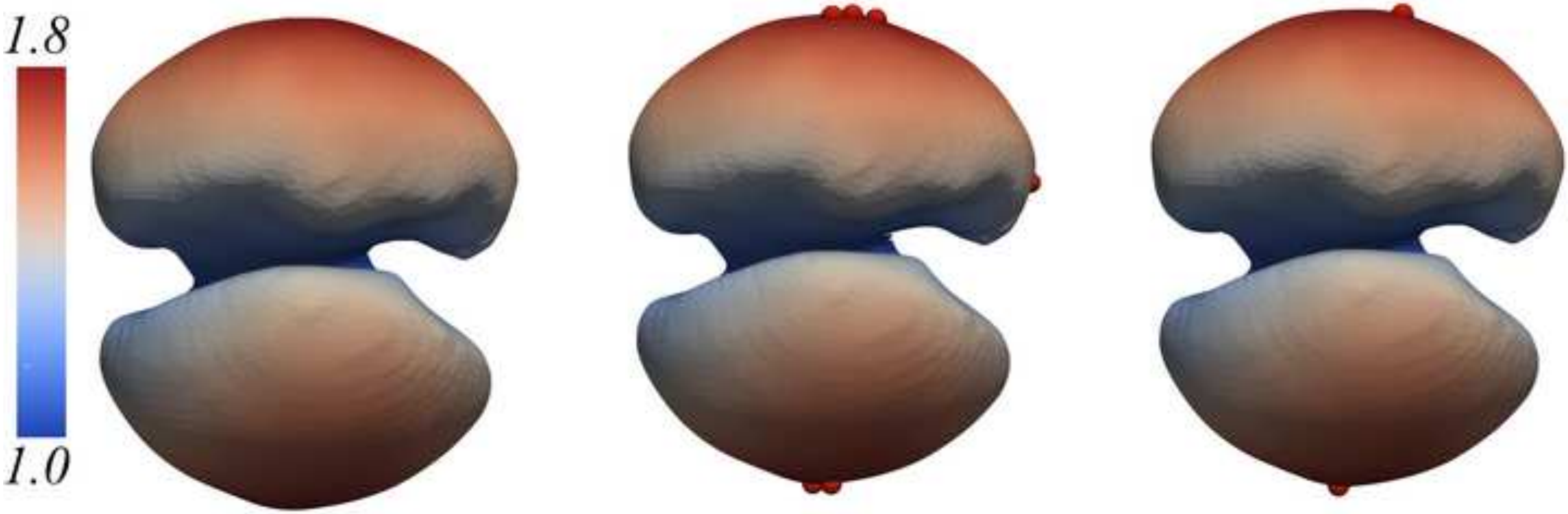

(a) (b) (c)

Figure 7

Click here to download high resolution image

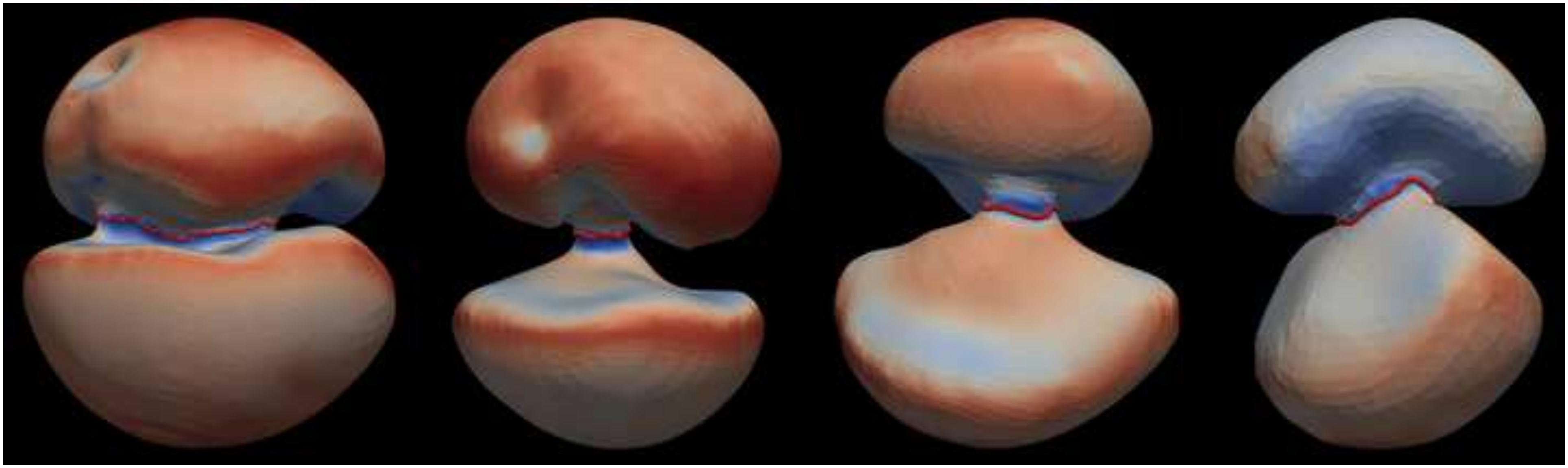

Figure 8

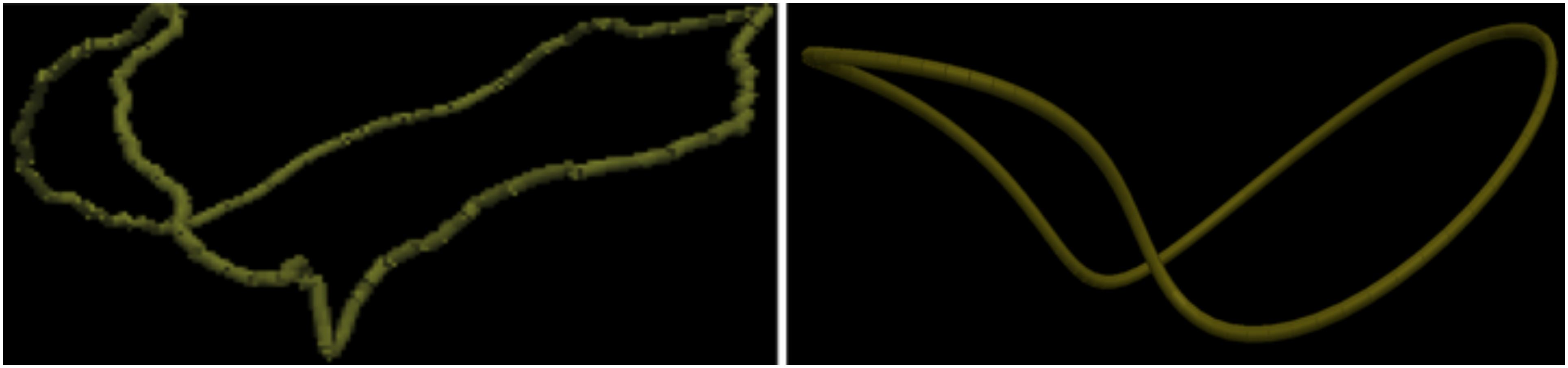

Figure 9

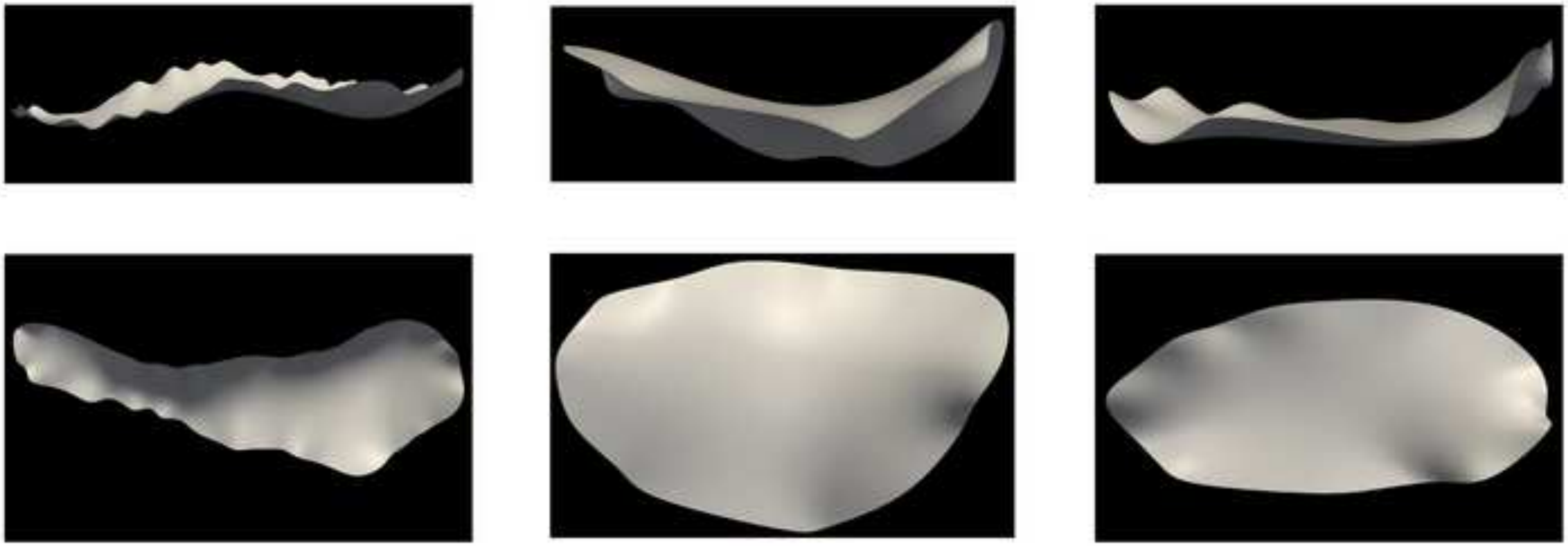

Figure 10

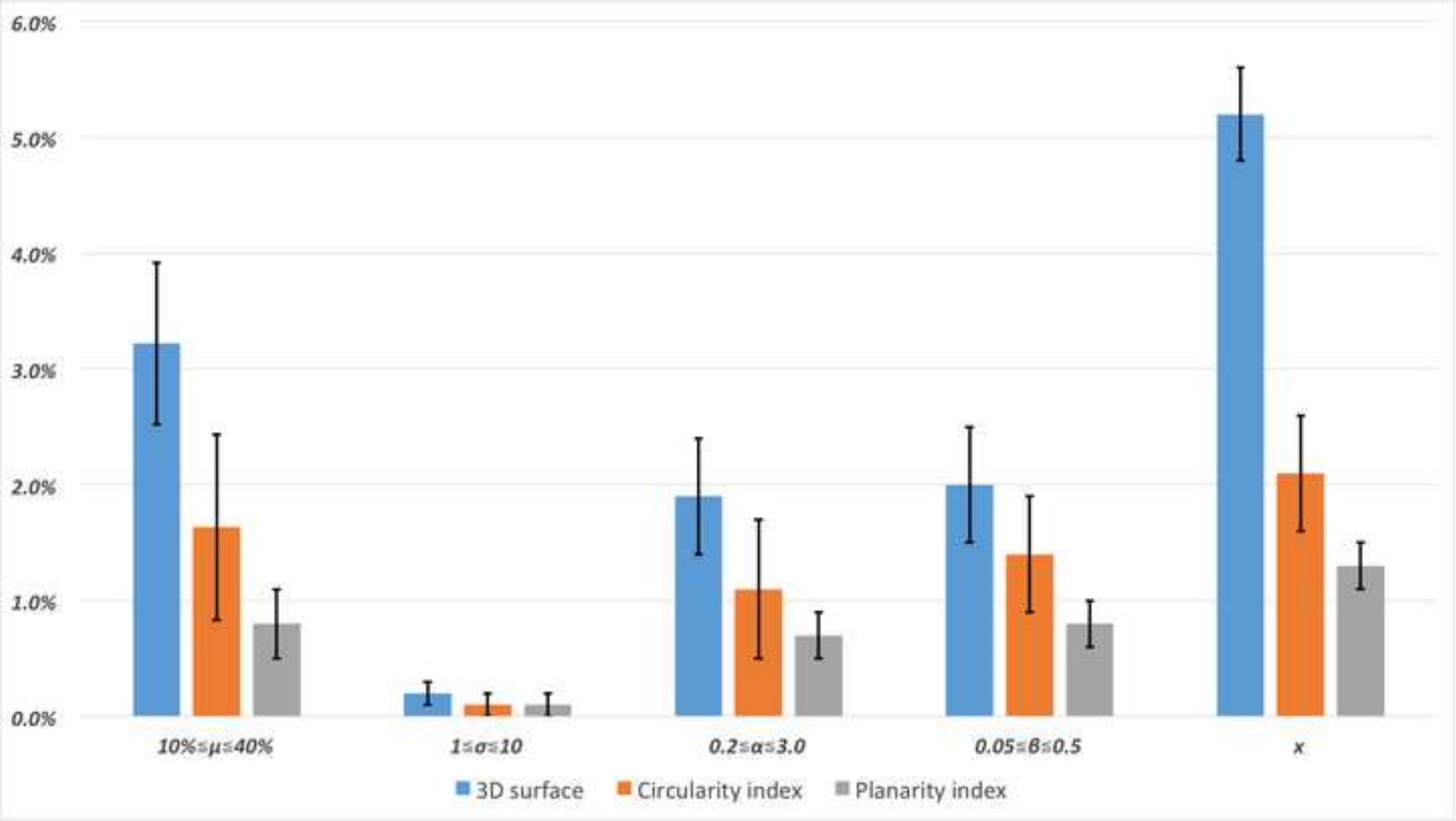
6.0%
5.0%
4.0%
3.0%
2.0%
1.0%
0.0%
10%≤μ≤40%
1≤σ≤10
0.2≤α≤3.0
0.05≤β≤0.5
x
3D surface
Circularity index
Planarity index

Figure 11

Click here to download high resolution image

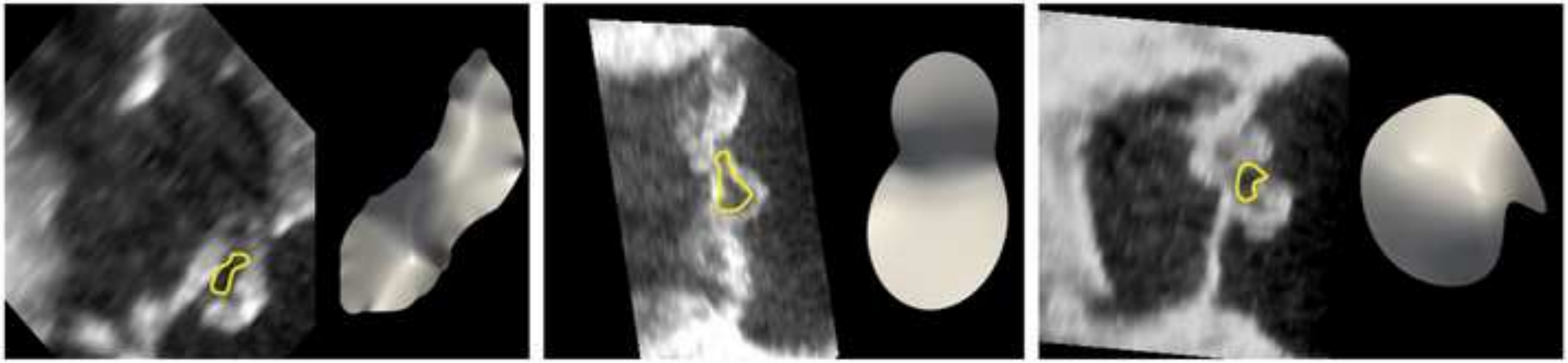

Figure 12

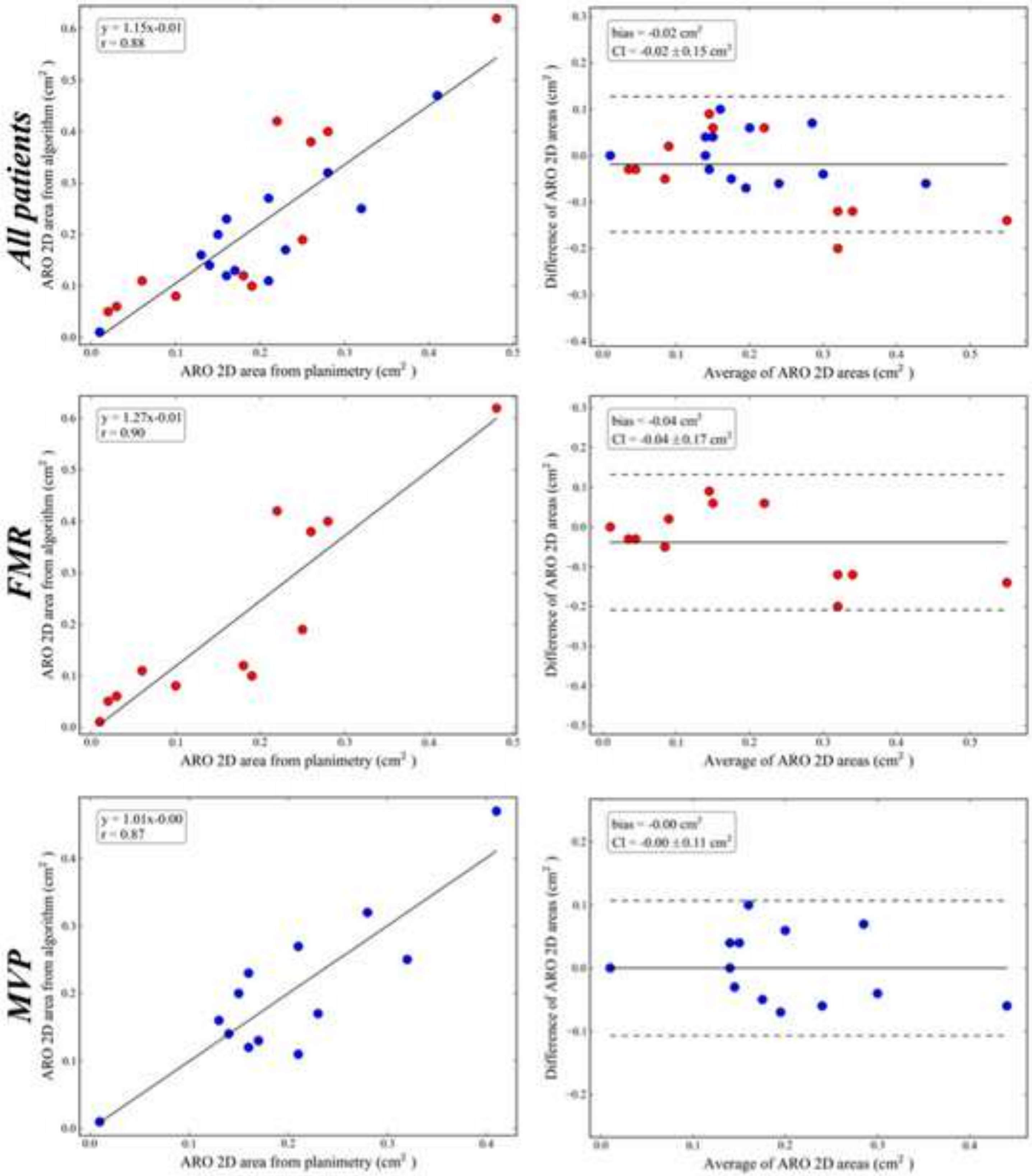
All patients
y = 1.15x-0.01
r = 0.88
ARO 2D area from algorithm (cm²)
ARO 2D area from planimetry (cm²)
bias = -0.02 cm²
CI = -0.02 ± 0.15 cm²
Difference of ARO 2D areas (cm²)
Average of ARO 2D areas (cm²)
FMR
y = 1.27x-0.01
r = 0.90
ARO 2D area from algorithm (cm²)
ARO 2D area from planimetry (cm²)
bias = -0.04 cm²
CI = -0.04 ± 0.17 cm²
Difference of ARO 2D areas (cm²)
Average of ARO 2D areas (cm²)
MVP
y = 1.01x-0.00
r = 0.87
ARO 2D area from algorithm (cm²)
ARO 2D area from planimetry (cm²)
bias = -0.00 cm²
CI = -0.00 ± 0.11 cm²
Difference of ARO 2D areas (cm²)
Average of ARO 2D areas (cm²)

Figure 13

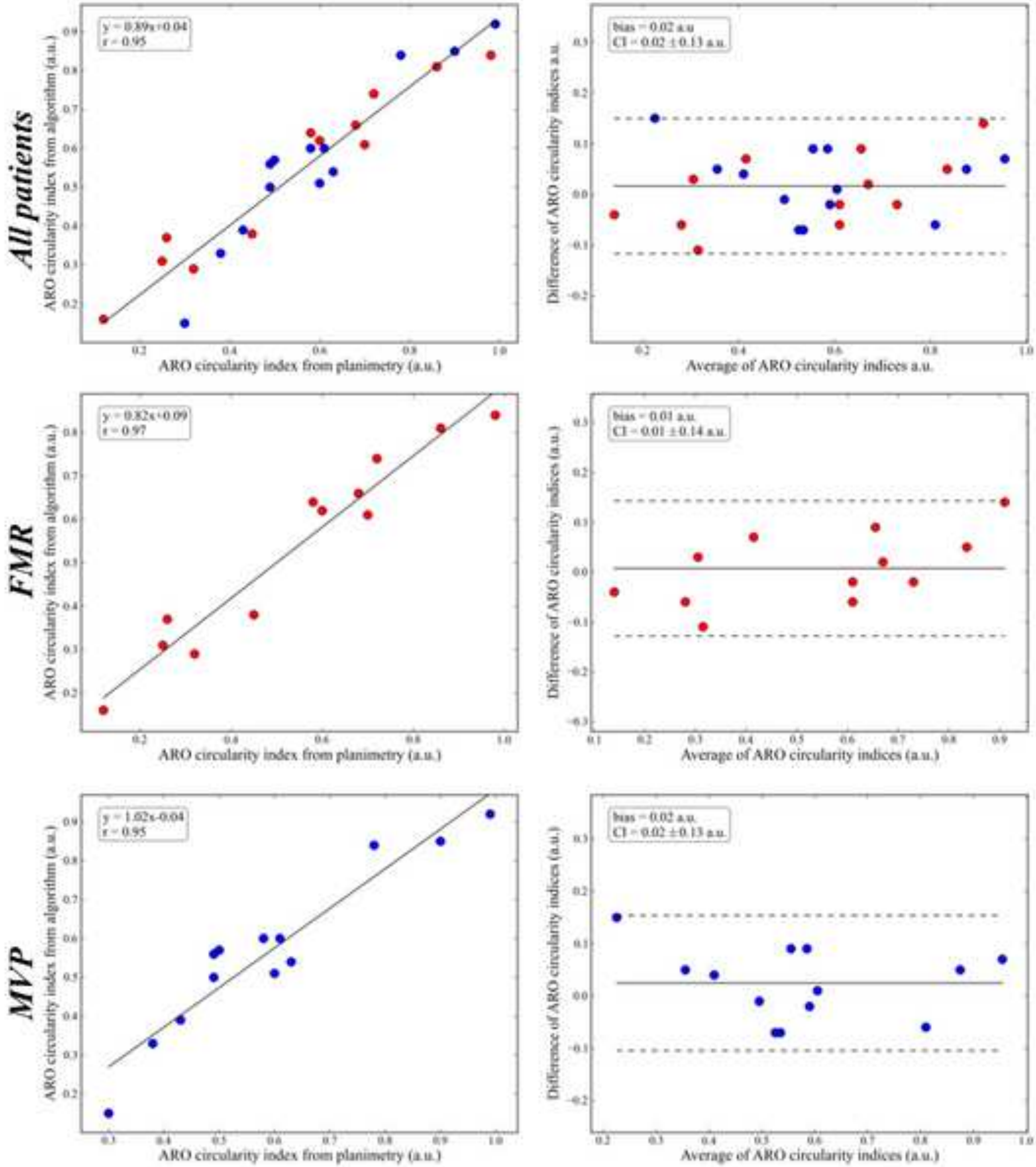
All patients
y = 0.89x+0.04
r = 0.95
ARO circularity index from algorithm (a.u.)
ARO circularity index from planimetry (a.u.)
bias = 0.02 a.u
CI = 0.02 ± 0.13 a.u.
Difference of ARO circularity indices a.u.
Average of ARO circularity indices a.u.
FMR
y = 0.82x+0.09
r = 0.97
ARO circularity index from algorithm (a.u.)
ARO circularity index from planimetry (a.u.)
bias = 0.01 a.u.
CI = 0.01 ± 0.14 a.u.
Difference of ARO circularity indices (a.u.)
Average of ARO circularity indices (a.u.)
MVP
y = 1.02x-0.04
r = 0.95
ARO circularity index from algorithm (a.u.)
ARO circularity index from planimetry (a.u.)
bias = 0.02 a.u.
CI = 0.02 ± 0.13 a.u.
Difference of ARO circularity indices (a.u.)
Average of ARO circularity indices (a.u.)